# Hexagonalization of Aluminogermanate Imogolite Nanotubes Organized Into Closed-Packed Bundles

**6 AUTHORS**, INCLUDING:

Erwan Paineau
French National Centre for Scientific Research
**31** PUBLICATIONS **307** CITATIONS

SEE PROFILE

Maria Bacia-Verloop
Institut de Biologie Structurale (IBS)
**38** PUBLICATIONS **324** CITATIONS

SEE PROFILE

Antoine Thill
Atomic Energy and Alternative Energies Com…
**74** PUBLICATIONS **1,286** CITATIONS

SEE PROFILE

Pascale Launois
French National Centre for Scientific Research
**140** PUBLICATIONS **2,189** CITATIONS

SEE PROFILE

# Hexagonalization of Aluminogermanate Imogolite Nanotubes Organized into Closed-Packed Bundles

Mohamed Salah Amara,[†,‡] Stéphan Rouzière,[†] Erwan Paineau,[†,‡] Maria Bacia-Verloop,[§] Antoine Thill,*,[‡] and Pascale Launois*,[†]

[†]Laboratoire de Physique des Solides, UMR CNRS 8502, Université Paris-Sud, Bâtiment 510, 91405 Orsay Cedex, France
[‡]Laboratoire Interdisciplinaire sur l'Organisation Nanométrique et Supramoléculaire, UMR CNRS 3299, CEA Saclay, 91191 Gif-sur-Yvette, France
[§]Institut de Biologie Structurale, UMR CNRS 5075, 41 rue Jules Horowitz, 38027 Grenoble, France

**S** *Supporting Information*

**ABSTRACT:** Imogolite nanotubes are promising building blocks for nanotechnologies with potential applications in molecular separation, molecular storage, or catalysis. We present an experimental study of the structure of germanium-based imogolite nanotubes $Al_2O_3Ge(OH)_4$ arranged in bundles. It combines cryo-transmission electron microscopy, infrared spectroscopy, thermogravimetric measurements, and X-ray scattering experiments. Thanks to a systematic method developed to analyze X-ray scattering diagrams as a function of the nanotube shape, single-walled germanium-based imogolite nanotubes, known as cylindrical for more than 30 years, are shown to take an hexagonal base shape when arranged in bundles. Physical and chemical properties of hexagonal imogolite nanotubes should markedly differ from those of cylindrical ones, making hexagonal basis nanotubes a "new" member, of particular interest, of the rich family of imogolites.
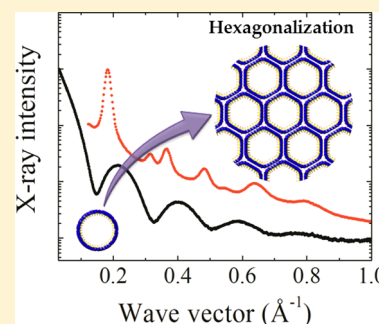
## 1. INTRODUCTION

The progress in experimental nanosciences and nanotechnologies is based on the development of their nano-building blocks. A huge variety of carbon nanoforms have been identified.[1] In parallel, the synthesis of inorganic metal oxide nanotubes and of inorganic fullerene-like nanoparticles is the subject of intense research.[2] Organic and inorganic cylindrical nanotubes are at the basis of an entire part of nanosciences and nanotechnologies. The most famous representatives of organic nanotubes are indisputably carbon nanotubes (CNT). Among inorganic nanotubes, imogolite nanotubes (INT) are probably the nanometric diameter nanotubes allowing for the best structural control. INTs[3] have nominal composition $Al_2O_3(Si_xGe_{1-x})(OH)_4$. They consist in isolated $[(OH)\text{-}Si_xGe_{1-x}O_3]$ tetrahedral units on the interior surface, connected to a curved gibbsite octahedral framework $[Al_2(OH)_3]$ on the outer surface.[4,5] These nanotubes are remarkable in several aspects. They can be synthesized easily and in large quantities by using low-temperature solution-phase chemistry methods,[6,7] larger yields (defined as the mass of nanotubes per milliliter of reaction volume) raising to up to 0.1 mol·L$^{-1}$. Compared to carbon nanotubes which require postsynthesis sorting procedures,[8,9] as-produced imogolite nanotubes are monodisperse in diameter and chirality. Indeed, their strain energy presents a well-defined minimum, chirality-dependent, as a function of the diameter, contrarily to carbon nanotubes where it decreases monotonically with increasing diameters.[10] Adjustment of the diameter has been achieved by substituting silicon by germanium,[5,11] and these germanium-based imogolite nanotubes (Ge-INT) can be produced not only as single-

walled (SW) nanotubes, but as well as double-walled (DW) nanotubes.[7,12−14] Typically, inner radii of synthetic imogolite nanotubes are equal to about 0.7 nm for SW Si-INT, 1.4 nm for SW Ge-INT, and 0.8 nm for DW Ge-INT. Alternatively, the use of different precursors of the synthesis was reported to lead to the formation of silicon-based nanotubes with tunable diameters.[6] The peculiar structure of INTs with inner and outer hydroxyl groups also makes them excellent candidates for surface modification. Hybrid INTs have been obtained by substituting the internal −OH layer with a −CH$_3$ one in SW silicon-based INTs,[15] resulting in increased methane adsorption capacities. Recently synthesized single-walled aminoalumonosilicate nanotubes, with up to 15% of the interior $\equiv$Si—OH groups substituted by $\equiv$Si—CH$_2$NH$_2$ groups, showed enhanced molecular adsorption selectivity.[16] On theoretical bases, other imogolite-like nanotubes have been considered by replacing tetrahedral silicate groups with phosphate, phosphite, arsenate, or arsenite units.[17] The rich family of imogolite nanotubes has interesting properties with respect to many different applications, including molecular separation,[18,19] molecular storage,[15,20,21] or catalysis.[22]

Drying of imogolite suspensions leads to the obtention of imogolite powders, where imogolite nanotubes can assemble in bundles.[23] Few works, mainly based on numerical simulations,[24,25] evidenced significant ovalization phenomena of nanotubes when organized in bundles. To probe the possible

deformation of nanotubes in bundles, we propose in this article an innovative experimental approach, allowing us to analyze the nanotube shape. The present work reports a multitechnique analysis of germanium-based imogolite nanotubes. We performed transmission electron microscopy (TEM), thermogravimetric analysis (TGA), infrared (IR) spectroscopy, and X-ray scattering (XRS) measurements. A systematic method is developed to analyze XRS diagrams as a function of the nanotube shape. We show that these imogolite nanotubes, considered as *cylindrical* nanotubes for more than 30 years now,[5] deform and take a *regular hexagonal shape* when arranged in large bundles. Finally, the radial deformation of imogolite nanotubes, compared to carbon nanotubes, is discussed. The physical and chemical properties of hexagonal-based imogolite nanotubes are expected to be markedly modified with respect to those of cylindrical ones, as will be argued below.

## 2. EXPERIMENTAL SECTION

**2.1. Synthesis of Aluminogermanate Nanotubes.** Tetraethoxygermanium was added to a 1 mol·L$^{-1}$ aqueous solution of aluminum perchlorate until an Al/Ge ratio of 2 was reached. Then, a 1 mol·L$^{-1}$ NaOH solution was slowly added to obtain an OH/Al ratio close to 2. The mixture was stirred overnight and heated at 90 °C in an oven for 20 days. Once the aging process is ended, the resultant mixture was cooled to ambient temperature. The suspension was then dialyzed with use of 10 kDa membranes. An aliquot of the dialyzed suspension was used for small-angle X-ray scattering investigations, while the rest of the suspension was dried at room temperature to obtain a powder of imogolite bundles.

**2.2. Infrared Spectroscopy.** The infrared spectrum was recorded with a Bruker Vertex 70 FTIR spectrometer at a resolution of 4 cm$^{-1}$ in transmission mode. A 1.5 mg sample of dried imogolite powder was mixed with 150 mg of potassium bromide powder and then pressed at $5 \times 10^8$ Pa into a transparent pellet. The IR spectrum was collected at room temperature by averaging 200 scans in the 4000−400 cm$^{-1}$ range.

**2.3. X-ray Scattering Measurements.** *2.3.1. Imogolite Suspension.* Imogolite suspensions were put in kapton capillaries of 2.6 mm diameter for X-ray scattering measurements, on an X-ray scattering setup including a rotating molybdenum anode and collimating optics providing a monochromatic beam of $1 \times 1$ mm$^2$ at the sample position. Incident wavelength is $\lambda = 0.709$ Å. A vacuum chamber behind the sample allows minimization of the small angle scattering signal of air. The transmitted flux was measured continuously with a photodiode placed in the beam stop. A MAR research X-ray sensitive 345 mm plate detector with 100 $\mu$m pixel size was placed behind the output window of the vacuum chamber, at a distance of 720 mm from the sample. Scattering vectors down to $Q_{min} = 0.03$ Å$^{-1}$ can be reached. Resolution was measured by using tetradecanol, whose diffraction peaks are very narrow: it is found to be a Gaussian function with half width at half maximum (fwhm) $\approx 0.013$ Å$^{-1}$.

*2.3.2. Imogolite Powder.* A 10 $\mu$m thick aluminum foil was wrapped around a few milligrams of imogolite powder, leading to a parallelepipedic sample. Its small side is parallel to the incident X-ray beam. Aluminum was chosen because its first diffraction peak is located at $Q \approx 2.7$ Å$^{-1}$, outside the $Q$-range studied in this work ($Q \leq 1$ Å$^{-1}$). X-ray scattering measurements were performed on a copper rotating anode generator, monochromatization ($\lambda = 1.542$ Å) being carried out

by a multilayer W/Si optics. X-ray diffraction diagrams were recorded on a MAR research X-ray sensitive 345 mm plate detector with 150 $\mu$m pixel size, placed after the sample at a distance of 273 mm. Resolution was measured with use of quartz and lead thiolate powders. Their diffraction peaks have been fitted by using a Gaussian function with fwhm $\approx 0.0135$ Å$^{-1}$. Homemade softwares allow for the angular grouping of measured intensities, to obtain scattering diagrams $I(Q)$ with high signal over background ratio.

**2.4. Thermogravimetric Analysis.** Thermogravimetric analysis was performed with a TGA Q50 (V20.10 Build 36) instrument. Approximately 20 mg of powder sample was heated under nitrogen gas flux from 25 to 1000 °C with a ramp of 10 deg/min. The weight loss in the text is normalized to the powder weight at 250 °C.

**2.5. Electron Microscopy.** Cryo-TEM experiments were undertaken with use of a FEI Tecnai G2 Polara device operating at 100 kV, under low electron illumination conditions (dose <15 e$^-$/Å$^2$). The images were collected by using a 4k × 4k Ultrascan Gatan camera with a calibrated magnification of 155 000. A drop (4 $\mu$L) of the solution was deposited on a R2/2 Quantifoil grid made hydrophilic after glow discharging. A fully automated Vitrobot (FEI) device was used to blot the grid and rapidly plunge and freeze aqueous films of the nanotubes suspensions into liquid ethane cooled by liquid nitrogen, to prevent the formation of ice crystals.

Imogolite powder was embedded in EMbed 812 resin (EMS) and polymerized for 24 h at 60 °C. This resin block was trimmed with Leica EM-Trim2 and ultrathin sections of 80 nm were made with use of a Leica UC7 and Diatome Ultra35 diamond knife. Sections were retrieved on carbonated 100 mesh copper grids. TEM observation was performed on Polara operating at 300 kV.

## 3. RESULTS

**3.1. Imogolite Suspension.** Synthesis being based on solution-phase chemistry, we first investigated the as-synthesized Ge-imogolite nanotubes in suspension. Figure 1 presents the XRS diagram of the suspension. Scattering intensity as a function of the wave-vector modulus $Q$ ($Q = 4\pi \sin(\theta_B)/\lambda$, $2\theta_B$ being the scattering angle and $\lambda$ the X-rays wavelength) exhibits
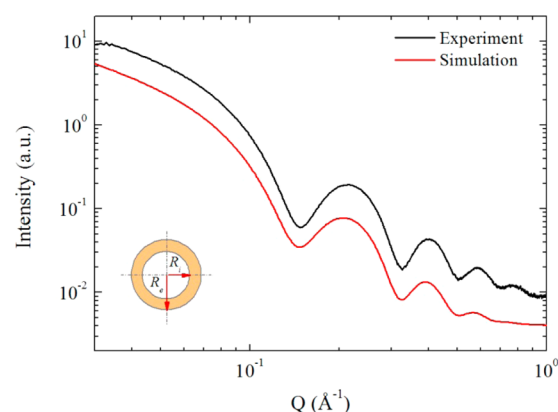


**Figure 1.** X-ray scattering diagram of as-synthesized Ge-imogolite nanotubes in suspension. Black line: experimental data. Red line: calculated curve, translated vertically for the sake of clarity. The inset represents a sketch of a single-walled nanotube with internal radius $R_i$ and external radius $R_e$.
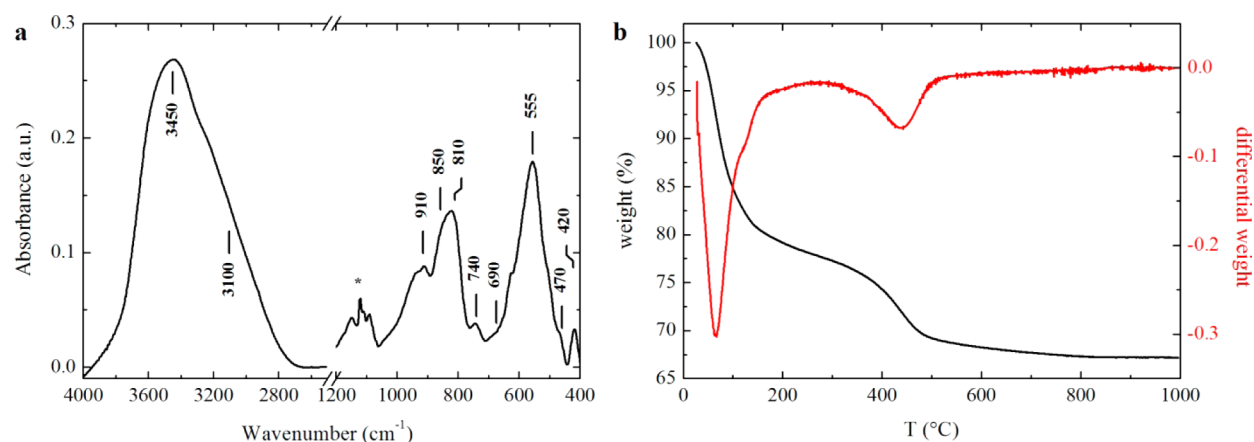
**Figure 2.** (a) Transmission IR spectrum of a transparent KBr pellet containing 1 wt % of Ge-imogolite powder. The star indicates characteristic vibrational bands of remaining perchlorate anions. (b) TGA (black) and differential TGA (red) curves obtained on the imogolite powder.
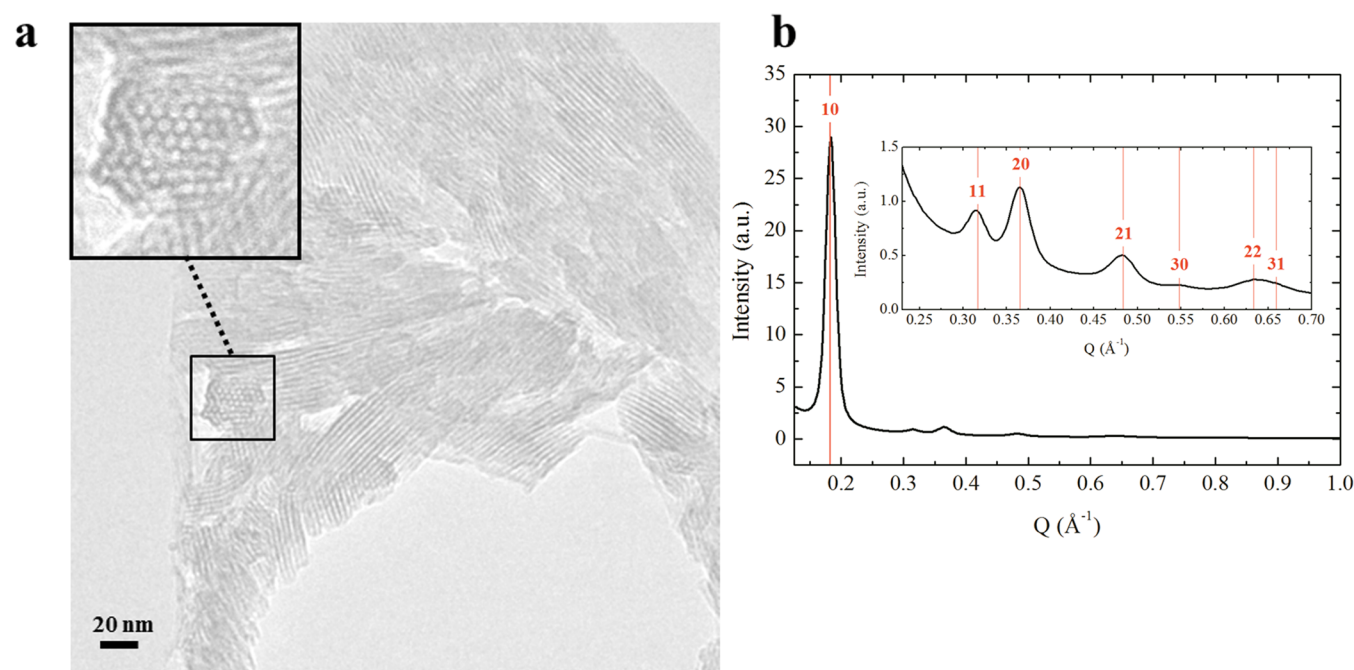


**Figure 3.** Imogolite powder: (a) TEM image and (b) experimental XRS diagram of the dehydrated imogolite powder at $T$ = 250 °C. The $hk$ indices refer to the positions of the 2D hexagonal reciprocal lattice peaks (red lines) of SW INTs bundles.

pronounced oscillations, characteristics of nanotubes monodisperse in diameter.[12,13]

Our study focusing on the $Q$-range below 1 Å$^{-1}$, XRS diagrams can be analyzed within the homogeneous approximation, i.e., with an homogeneous electron density.[26] The model used is detailed in the Supporting Information and a calculated scattering diagram is reported in Figure 1. Quantitative agreement between experiment and calculation is obtained considering that the suspension is made of cylindrical SW nanotubes with internal radius $R_i$ =13.8 Å and external radius $R_e$ =20.3 Å (wall thickness = 6.5 Å). The presence in the suspension, in minor proportions, of DW nanotubes and of proto-imogolites, which are small tiles prefiguring nanotubes formation,[27] can also be deduced from the analysis of the XRS diagram. Relative weight fractions of SW nanotubes, DW nanotubes, and proto-imogolites are found to be 86.1, 9.3, and 4.6 wt %, respectively. Cryo-TEM images of the frozen suspension confirm the presence of a majority of SW

nanotubes, with few DW nanotubes and remaining proto-imogolites (Figure S1 in the Supporting Information).

**3.2. Imogolite Powder.** Further analyses were made on powder after evaporation of the suspension at room temperature. Figure 2a represents the infrared (IR) spectrum of the INTs powder mixed with KBr to obtain a transparent pellet.

The large absorption band in the OH stretching region corresponds to external Al(OH)Al (4000−3200 cm$^{-1}$) and internal GeOH (3200−2800 cm$^{-1}$) groups.[15] At lower wavenumbers, the two bands located at 910 and 810 cm$^{-1}$ are assigned to Al−O−Ge stretching vibrations in agreement with previous works[5,11] while the region around 850 cm$^{-1}$ has been ascribed to an OH-related vibration.[5] The bands located at 555 and 420 cm$^{-1}$ are characteristic of the INT structure and arise from various Al−O stretching vibrations.[5] Finally, it has been recently shown that SW and DW structures can be distinguished by their IR spectrum.[13] Indeed, SW Ge-INTs present an Al−O stretching vibration located at 740 cm$^{-1}$ while
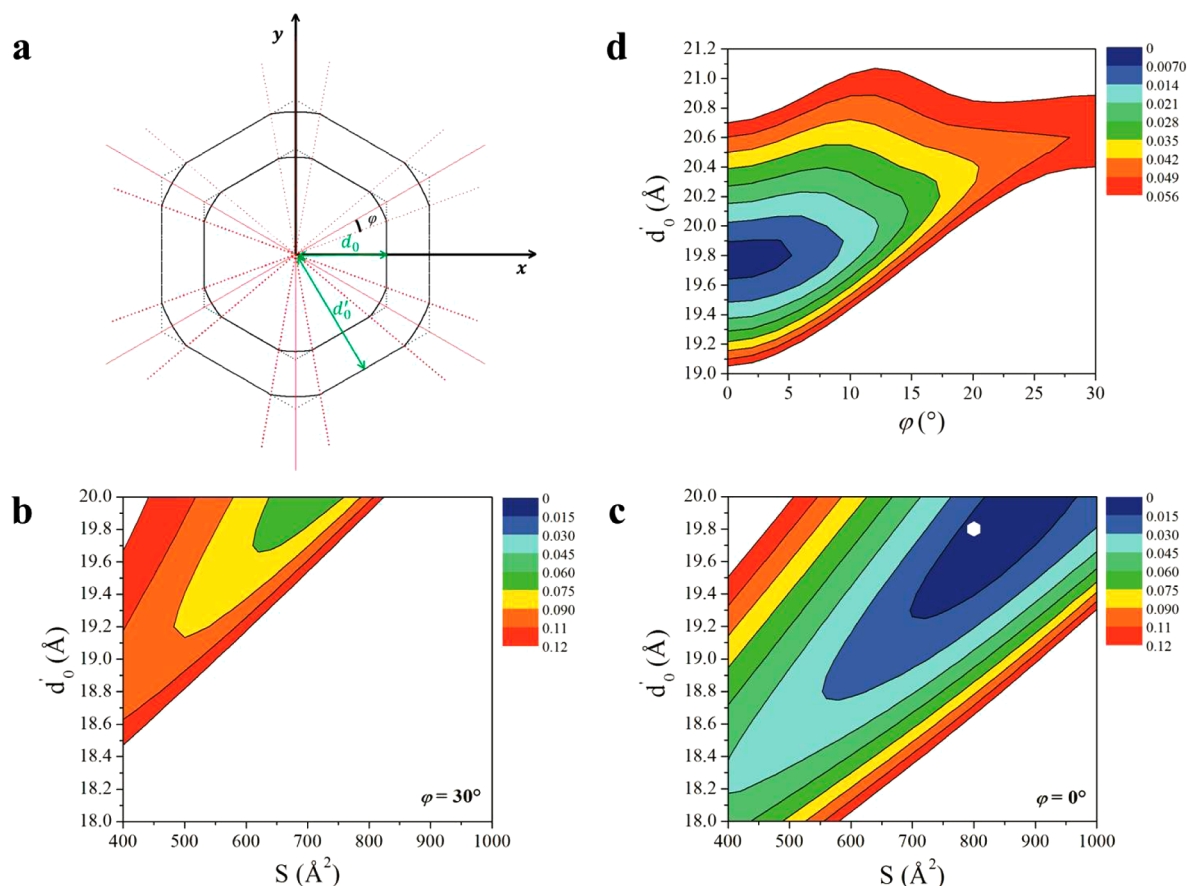
**Figure 4.** (a) Shape of a deformed single-walled imogolite nanotube, within the homogeneous approximation. (b, c) Evolution of the standard deviation parameter $\Delta$ as a function of $d_0'$ and of the surface $S$ for $\varphi = 30°$ (cylindrical nanotube) and $0°$ (hexagonal nanotube). (d) Evolution of the standard deviation parameter $\Delta$ as a function of $d_0'$ and $\varphi$ for a constant surface $S = 820$ Å².

this peak is absent for DW Ge-INTs, two new absorption bands being then observed at 470 and 690 cm$^{-1}$. The presence of weak shoulders at 470 and 690 cm$^{-1}$ therefore indicates that a small proportion of DW Ge-INTs remains in our sample. In summary, IR measurements corroborate the conclusions of SAXS analysis, revealing that our INTs powder is mainly composed of SW imogolite nanotubes.

Thermogravimetric analysis (TGA) measurements performed on the imogolite powder are reported in Figure 2b. Weight losses occurring at 65 and 130 °C correspond to dehydration phenomena, while dehydroxylation takes place around 450 °C. Therefore, the INTs powder can be considered as fully dehydrated at 250 °C with an endothermic weight loss of ∼28% water. Similar results were obtained for Si-INTs.[28,29]

TEM images as the one in Figure 3a clearly show that INTs are closely packed in bundles, as single walled carbon nanotubes can be.[30]

It has been proposed that a weak positive charge is developed on the external surface of imogolite nanotubes.[31,32] Consequently, counterions present in the synthesis solution for sake of electroneutrality should intercalate between the nanotubes upon drying in order to avoid any repulsion. This hypothesis is confirmed by the IR spectrum of the dried sample in Figure 2a, which displays absorption peaks at ∼1100 cm$^{-1}$, characteristic of the Cl−O vibrational bands from the perchlorate anions, which was in fact present in previous samples obtained by using the perchlorate synthesis route.[33,34] Zoom on a bundle of nanotubes pointing upward (inset in Figure 3a) indicates that

nanotubes are organized on a two-dimensional (2D) hexagonal lattice. We will now focus on the dehydrated powder to examine the fate of INT shape in bundles. We performed a detailed structural study, based on X-ray scattering experiments realized at 250 °C, in order to avoid interference effects between water molecules inside and around the nanotubes and the nanotubes themselves. Indeed, such interferences induce strong modifications of XRS diagrams, as discussed, e.g., in references 29 and 35, making the present analysis of nanotube shape much more difficult. The XRS diagram presents diffraction peaks located at the $hk$ positions of a 2D hexagonal lattice, as shown in Figure 3b. The hexagonal lattice parameter $a$ can thus be determined by

$$a = \left\langle \sqrt{h^2 + k^2 + hk} \, \frac{4\pi}{\sqrt{3} \, Q_{hk}} \right\rangle \qquad (1)$$

where $Q_{hk}$ refers to the position of the diffraction peak of Miller indices $hk$. By using eq 1 for 10, 11, 20, 21, and 30 peaks, $a$ is found equal to 39.7 Å. For bundles formed of a small number of nanotubes, as was shown for carbon nanotubes,[26,30] peak positions could deviate from the ones given by eq 1, which is strictly valid for an infinite lattice only; their widths increase with decreasing bundle size. For our Ge-INT sample, measured widths correspond to about ∼60 tubes per bundle, as will be shown below when comparing the experimental diagram to a calculated one. Peak shifts are reduced for such large bundles. The above-mentioned value of 39.7 Å also corresponds to the

best agreement between the experimental diagram and calculated ones. The number of tubes per bundles found from calculations is in good agreement with TEM observations (inset of Figure 3a). Finally, one should underline that diffraction peak positions are all indexed by using only one tube−tube distance and correspond to the organization of the predominant SW nanotubes. The minority DW and proto-imogolite entities do not self-organize and only contribute to the small background signal in Figure 3b.

Assuming a cylindrical shape of the INTs as in the suspension, the distance between two adjacent nanotubes in a bundle should be larger than two times their external radius ($2R_e = 40.6$ Å). Larger effective radii should even be considered if one takes into account the size of perchlorate anions intercalated between the nanotubes. Nevertheless, XRS experiment on the dehydrated powder gives a lattice parameter $a = 39.7$ Å, which is significantly smaller than the expected one (above 40.6 Å). It reveals that INTs no longer have a cylindrical shape. Quantitative modeling of INT deformation will now be discussed.

**3.3. Deformation Modeling.** The model used to account for nanotube deformation perpendicularly to its axis, within the homogeneous approximation used in this article, is presented in Figure 4a. Starting from the cylindrical shape, we have assumed that the nanotube section consists of a *rounded-hexagonal* surface, which allows it to accommodate smaller lattice parameters and which respects the hexagonal symmetry of the 2D lattice. Rounded parts have an angular aperture of $2\varphi$ ($\varphi \in [0, 30°]$) and flat parts in between are characterized by internal and external apothems $d_0$ and $d_0'$. Thereby, for $\varphi = 30°$, the nanotube is cylindrical ($R_i = d_0$ and $R_e = d_0'$), while for $\varphi = 0°$, the INT is fully hexagonalized. Other deformations than the rounded-hexagonal shape can be ruled out because they would imply either (i) a distortion of the lattice from hexagonal, in contradiction with experimental data, or (ii) introduction of orientational disorder, which would lead to an increase of the lattice parameter, in contradiction with our determination of a smaller value than the one expected for cylindrical nanotubes.

The measured XRS diffraction peaks in Figure 3b are fitted with Gaussian line-shaped functions. Maximum intensities $I_{exp}$ of peaks 10, 11, 20, 21, and 22/31 (not separated due to peaks overlapping) are rated by integers ranging from 0 to 4. One defines, for $i = 1-4$ (corresponding to $hk = 11, 20, 21, 22/31$), $r_{exp}[i] = I_{exp}[i]/I_{exp}[0]$. The formalism we developed for calculating XRS diagrams is detailed in the Supporting Information.[35−37] Briefly, for a powder of bundles of nanotubes, the calculated intensity, prior to geometrical, polarization, absorption corrections and convolution to resolution, is

$$\tilde{I}(Q) \propto \frac{\tilde{\rho}_{imo}(Q)^2}{Q} \int_0^{2\pi} d\varphi_{\vec{Q}_\parallel} [|F_{\varphi,d_0,d_0'}(\vec{Q}_\parallel)|^2 \cdot \sum_{i,j \in bundle} \cos(\vec{Q}_\parallel \cdot \vec{R}_{ij})]$$

(2)

In this equation, the vectors $\vec{R}_{ij}$ join the centers of tubes $i$ and $j$ in a bundle in the plane perpendicular to its axis, $Q$ is the modulus of the wave-vector $\vec{Q}$, $\vec{Q}_\parallel$ is its component in the plane perpendicular to the bundle axis, and $\varphi_{\vec{Q}_\parallel}$ is the angle between $\vec{Q}_\parallel$ and the $x$ axis in Figure 4a. The form factor $F_{\varphi,d_0,d_0'}(\vec{Q}_\parallel)$ is the Fourier transform of the nanotube surface in Figure 4a and $\tilde{\rho}_{imo}(Q)$ is the imogolite form factor renormalized to its electronic density, as defined in the Supporting Information.

Calculated XRS intensities depend on three parameters $\varphi$, $d_0$, and $d_0'$ or, equivalently $\varphi$, $d_0'$, and $S$, where

$$S = 6(d_0'^2 - d_0^2)\left[\frac{\varphi}{\cos^2\left(\frac{\pi}{6} - \varphi\right)} + \tan\left(\frac{\pi}{6} - \varphi\right)\right]$$

(3)

is the surface of the nanotube in Figure 4a, with $\varphi$ in radians. In the following, we propose a systematic method to determine the nanotube shape, allowing for the best fit of experimental data. For each value of the triplet of parameters $\varphi$, $d_0'$, and $S$, we simulate XRS intensity using a homemade program that returns calculated maximum intensities $I_{calc}[i]$ ($i = 0-4$) around 10, 11, 20, 21, and 22/31 peak positions. The hexagonal lattice parameter is fixed to the value deduced from experiments $a = 39.7$ Å. Calculations are performed for ~60 tubes per bundle which give peak widths similar to experimental ones, as illustrated in Figure 5 and in Figure S5 in the Supporting Information
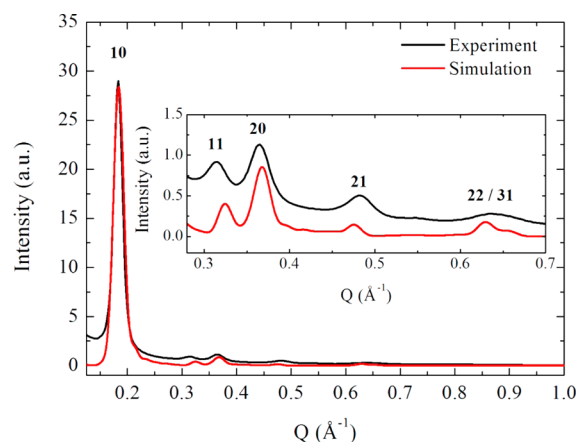


**Figure 5.** Experimental and calculated XRS diagrams of the dehydrated powder of imogolite nanotubes. Calculation is done for $\varphi = 0°$, $d_0 = 12.7$ Å, and $d_0' = 19.8$ Å ($S = 830$ Å$^2$), corresponding to the white hexagonal symbol in Figure 4c.

We defined for $i = 1-4$, $r_{calc}[i] = I_{calc}[i]/I_{calc}[0]$. Intensities are renormalized to the intensity of the most intense peak ($hk = 10$) in order to minimize the background contribution. Comparison between experimental and calculated data is evaluated by using the standard deviation $\Delta(\varphi,d_0',S) = \{\sum_{i=1}^4 (r_{exp}[i] - r_{calc}[i])^2\}^{1/2}$. Variation of the standard deviation parameter $\Delta$ as a function of the external apothem $d_0'$ and of the surface $S$ of the nanotube is shown in Figure 4b and Figure 4c for $\varphi = 30°$ (circular nanotube) and for $\varphi = 0°$ (hexagonal nanotube), respectively. The case of intermediate round-hexagonal tubes is presented in Figure S4 in the Supporting Information. The absolute minimum in $\Delta$ is obtained for $\varphi = 0°$, that is for hexagonalized nanotubes. The surface of the nanotube perpendicularly to its long axis is found to be $S \approx 800$ Å$^2$. It is larger than the surface of an isolated cylindrical nanotube in solution $S_0 = \pi(R_e^2 - R_i^2) \approx 700$ Å$^2$, which is attributed to the presence of perchlorate anions at the surface of the nanotubes in the dried powder. Indeed, within the homogeneous approximation, perchlorate anions correspond to an outer shell of electronic density around the tube, leading to a larger effective surface. Variation of $\Delta$ for a NT constant surface, as a function of the external apothem $d_0'$ and of the angle $\varphi$, is drawn in Figure 4d. The absolute minimum in $\Delta$

corresponds to $d_0' \approx 19.8$ Å, which is compatible with the measured lattice parameter ($a \approx 2d_0'$). Finally, Figure 5 represents a comparison between experimental and calculated XRS diagrams, for hexagonalized nanotubes.

Similar calculations for cylindrical nanotubes are presented in Figure S5 in the Supporting Information. As expected, good agreement is obvious with hexagonal deformation (Figure 5) whereas the cylindrical shape fails to reproduce the experimental intensities (Figure S5 in the Supporting Information).

In summary, stringent comparison between experimental and calculated XRS diagrams unambiguously shows that imogolite nanotubes assembled in large bundles on an hexagonal lattice are strongly deformed, from their initial *cylindrical* shape to an *hexagonal* one. To the best of our knowledge, our study provides the first experimental evidence of such a deformation of an imogolite nanotube. Moreover, within the homogeneous approximation, the nanotubes are found to have a perfect hexagonal cross section, corresponding to the largest deviation from circular shape considered in Figure 4a.

## 4. DISCUSSION

As noted in the Introduction, carbon and imogolite nanotubes may be considered as archetypes of organic and inorganic nanotubes, respectively. There is already quite a bit of literature about CNTs deformation (see references 38−43 and references therein). Carbon nanotubes, although they present extremely high axial Young's modulus of about 2 GPa, can undergo radial deformations induced by relatively small forces. CNTs in-plane deformations depend on their diameter, on applied external pressure, and on the way they are organized against each other. In particular, at atmospheric pressure, CNTs organized on an hexagonal lattice can adopt the round-hexagonal shape for 17 Å diameter,[40] while they are found to be quite circular for 14 Å diameter.[39] Above a few nanometers diameter, nanotubes collapse to give a "dog-bone" cross section.[43] A rich deformation phase diagram has been proposed by Sluiter and Kawazoe.[41] Carbon nanotube deformations result from a delicate balance between intertube interactions and intratube radial elasticity. In the case of imogolite nanotubes, interactions between tubes are not yet sufficiently understood in the literature to be discussed in detail here. In particular, although the role of counterions in the bundling phenomenon has been pointed out by Gustaffson,[31] the impact of salts has not been considered in simulation studies.[24,25] It can, however, be inferred from Radial Breathing Modes frequency values calculated for imogolite nanotubes[10,11] that these nanotubes are rather soft. It is indeed what we show experimentally on Ge-based INT with internal and external radii of 13.8 and 20.3 Å, respectively, since we found them to be *fully* hexagonalized when assembled in large bundles. Moreover, as underlined in ref 44 for Si-INT, imogolite nanotube walls may contain different types of defect structures arising from atomic vacancies. Such defects/vacancies, if present in Ge-INT, could play a role in sustaining the hexagonal shape. Atomistic simulations would thus be most helpful to figure out which local distorsions are associated with hexagonalization. One may also note that Tamura and Kawamura[24] showed that when three Si-based nanotubes interact together, their shapes change and they become elliptical. Accordingly, Creton and co-workers[25] attest that few interacting Si-based imogolite nanotubes adopt elliptical cross sections, especially when dried, at low water densities. These analyses are performed for imogolite packings composed by few nanotubes. It might thus be possible that SW Si-based imogolite nanotubes hexagonalize when organized in large bundles, as is found for SW Ge-INTs. Further experimental studies are needed on large assemblies of Si-INTs. Another striking question concerns the behavior of double-walled Ge-based imogolite nanotubes that were discovered a few years ago:[12] are they sufficiently soft to deform when assembled in large bundles or will they always present circular cross sections?

Finally, we should underline the consequences of hexagonalization on the properties of imogolite nanotubes. From the mechanical point of view, in-plane compressibility of INTs bundles may be drastically increased by hexagonalization, as already predicted for carbon nanotubes.[38,40] Moreover, hexagonalization of imogolite nanotubes could induce strong modifications on INTs properties in terms of molecular separation,[18,19] molecular storage,[15,20,21] or catalysis,[22] as can be inferred from molecular dynamics and Monte Carlo analyses already published in the literature. In the case of Si-INT, Creton and co-workers[25] showed that the shapes of the nanotubes influence their electrostatic potential and thus determine the places of favorable adsorption. Such an effect, predicted on ovalized nanotubes, should be even more important for fully hexagonalized ones. In the same spirit, one may refer to Zang and co-workers study.[19] Indeed, the hexagonalization process of Ge-INT should modify the hydroxyl groups properties and these authors demonstrated that the flexibility of the hydroxyl groups on the inner surface of Si-imogolite nanotubes is critical in the adsorption of hydrogen-bonding molecules.

## 5. CONCLUSIONS

Single-walled imogolite nanotubes $Al_2O_3Ge(OH)_4$, when self-assembled in large bundles on a 2D hexagonal lattice, present an hexagonal cross section instead of a circular one. This first evidence for hexagonalization of imogolite nanotubes has been made possible thanks to a careful X-ray structural analysis. It should be interesting to pursue similar analyses on DW Ge-based nanotubes, on SW Si-based nanotubes, and on $Si_xGe_{1-x}$ nanotubes, in order to obtain more insight into their intra- and intertube interactions. Moreover, bundles of fully hexagonalized Ge-based SW nanotubes form a honeycomb material that is expected to present new mechanical and physicochemical properties. In particular, physicochemical properties of hexagonalized nanotubes in terms of adsorption or catalysis should be markedly different from those of circular ones. It is a safe bet that hexagonal imogolite nanotubes will motivate new experimental, numerical, and theoretical investigations.

## ■ ASSOCIATED CONTENT

### ⓢ Supporting Information

Details of the models used to simulate the scattering diagrams of imogolite nanotubes in solution or assembled in bundles, depending on their shape plus additional TEM image and supplementary simulation results. This material is available free of charge via the Internet at http://pubs.acs.org.

## ■ AUTHOR INFORMATION

### Corresponding Authors
*E-mail: pascale.launois@u-psud.fr. Tel: +33 (0)1 69 15 60 56.
*E-mail: antoine.thill@cea.fr. Tel: +33 (0)1 69 08 99 82.

# ■ REFERENCES

(1) Suarez-Martinez, I.; Grobert, N.; Ewels, C. P. Nomenclature of sp$^2$ Carbon Nanoforms. *Carbon* **2012**, *50*, 741−747.

(2) Tenne, R.; Redlich, M. Recent Progress in the Research of Inorganic Fullerene-Like Nanoparticles and Inorganic Nanotubes. *Chem. Soc. Rev.* **2010**, *39*, 1423−1434.

(3) Yoshinaga, N.; Aomine, S. Imogolite in some Ando Soils. *Soil Sci. Plant Nutr.* **1962**, *8*, 22−29.

(4) Cradwick, P.; Farmer, V.; Russell, J.; Masson, C.; Wada, K.; Yoshinaga, N. Imogolite, a Hydrated Aluminium Silicate of Tubular Structure. *Nature (London), Phys. Sci.* **1972**, *240*, 187−189.

(5) Wada, S.; Wada, K. Effects on Substitution of Germanium for Silicon in Imogolite. *Clays Clay Miner.* **1982**, *30*, 123−128.

(6) Yucelen, G.; Kang, D.; Guerrero-Ferreira, R.; Wright, E.; Beckham, H.; Nair, S. Shaping Single-Walled Metal Oxide Nanotubes from Precursors of Controlled Curvature. *Nano Lett.* **2012**, *12*, 827−832.

(7) Amara, M.-S.; Paineau, E.; Bacia-Verloop, M.; Krapf, M.-E.; Davidson, P.; Belloni, L.; Levard, C.; Rose, J.; Launois, P.; Thill, A. Single Step Formation of Micron Long (OH)$_3$Al$_2$O$_3$Ge(OH) Imogolite-Like Nanotubes. *Chem. Commun.* **2013**, *49*, 11284−11286.

(8) Subbaiyan, N. K.; Cambré, S.; Parra-Vasquez, A. N. G.; Hároz, E. H.; Doorn, S. K.; Duque, J. G. Role of Surfactants and Salt in Aqueous Two-Phase Separation of Carbon Nanotubes Towards Simple Chirality Isolation. *ACS Nano* **2014**, *8*, 1619−1628.

(9) Fagan, J. A.; Khripin, C. Y.; Silvera Batista, C. A.; Simpson, J. R.; Hároz, E. H.; HightWalker, A. R.; Zheng, M. Isolation of Specific Small-Diameter Single-Wall Carbon Nanotube Species via Aqueous Two-Phase Extraction. *Adv. Mater.* **2014**, DOI: 10.1002/adma.201304873.

(10) Guimarães, L.; Enyashin, A.; Frenzel, J.; Heine, T.; Duarte, H.; Seifert, G. Imogolite Nanotubes: Stability, Electronic, and Mechanical Properties. *ACS Nano* **2007**, *1*, 362−368.

(11) Konduri, S.; Mukherjee, S.; Nair, S. Controlling Nanotube Dimensions: Correlation between Composition, Diameter, and Internal Energy of Single-Walled Mixed Oxide Nanotubes. *ACS Nano* **2007**, *1*, 393−402.

(12) Maillet, P.; Levard, C.; Larquet, E.; Mariet, C.; Spalla, O.; Menguy, N.; Masion, A.; Doelsch, E.; Rose, J.; Thill, A. Evidence of Double-Walled Al-Ge Imogolite-Like Nanotubes. A Cryo-TEM and SAXS Investigation. *J. Am. Chem. Soc.* **2010**, *132*, 1208−1209.

(13) Thill, A.; Maillet, P.; Guiose, B.; Spalla, O.; Belloni, L.; Chaurand, P.; Auffan, M.; Olivi, L.; Rose, J. Physico-Chemical Control over the Single-or Double-Wall Structure of Aluminogermanate Imogolite-like Nanotubes. *J. Am. Chem. Soc.* **2012**, *134*, 3780−3786.

(14) Lourenço, M. P.; Guimarães, L.; Da Silva, M. C.; Oliveira, C. d.; Heine, T.; Duarte, H. A. Nanotubes with Well-Defined Structure: Single-and Double-Walled Imogolites. *J. Chem. Phys. C* **2014**, *118*, 5945−5953.

(15) Bottero, I.; Bonelli, B.; Ashbrook, S.; Wright, P.; Zhou, W.; Tagliabue, M.; Armandi, M.; Garrone, E. Synthesis and Characterization of Hybrid Organic/Inorganic Nanotubes of the Imogolite Type and their Behaviour Towards Methane Adsorption. *Phys. Chem. Chem. Phys.* **2011**, *13*, 744−750.

(16) Kang, D.-Y.; Brunelli, N. A.; Yucelen, G. I.; Venkatasubramanian, A.; Zang, J.; Leisen, J.; Hesketh, P. J.; Jones, C. W.; Nair, S. Direct Synthesis of Single-Walled Aminoaluminosilicate Nanotubes with Enhanced Molecular Adsorption Selectivity. *Nat. Commun.* **2014**, *5*, 3342.

(17) Guimarães, L.; Pinto, Y. N.; Lourenço, M. P.; Duarte, H. A. Imogolite-Like Nanotubes: Structure, Stability, Electronic and Mechanical Properties of the Phosphorous and Arsenic Derivatives. *Phys. Chem. Chem. Phys.* **2013**, *15*, 4303−4309.

(18) Zang, J.; Konduri, S.; Nair, S.; Sholl, D. S. Self-Diffusion of Water and Simple Alcohols in Single-Walled Aluminosilicate Nanotubes. *ACS Nano* **2009**, *3*, 1548−1556.

(19) Zang, J.; Chempath, S.; Konduri, S.; Nair, S.; Sholl, D. S. Flexibility of Ordered Surface Hydroxyls Influences the Adsorption of Molecules in Single-Walled Aluminosilicate nanotubes. *J. Phys. Chem. Lett.* **2010**, *1*, 1235−1240.

(20) Ohashi, F.; Tomura, S.; Akaku, K.; Hayashi, S.; Wada, S. Characterization of Synthetic Imogolite Nanotubes as Gas Storage. *J. Mater. Sci.* **2004**, *39*, 1799−1801.

(21) Zanzottera, C.; Armandi, M.; Esposito, S.; Garrone, E.; Bonelli, B. CO$_2$ Adsorption on Aluminosilicate Single-Walled Nanotubes of Imogolite Type. *J. Phys. Chem. C* **2012**, *116*, 20417−20425.

(22) Bonelli, B.; Bottero, I.; Ballarini, N.; Passeri, S.; Cavani, F.; Garrone, E. IR Spectroscopic and Catalytic Characterization of the Acidity of Imogolite-based Systems. *J. Catal.* **2009**, *264*, 15−30.

(23) Wada, K.; Yoshinaga, N. The Structure of "Imogolite". *Am. Mineral.* **1969**, *54*, 50−71.

(24) Tamura, K.; Kawamura, K. Molecular Dynamics Modeling of Tubular Aluminum Silicate: Imogolite. *J. Phys. Chem. B* **2002**, *106*, 271−278.

(25) Creton, B.; Bougeard, D.; Smirnov, K.; Guilment, J.; Poncelet, O. Molecular Dynamics Study of Hydrated Imogolite. *Phys. Chem. Chem. Phys.* **2008**, *10*, 4879−4888.

(26) Rols, S.; Almairac, R.; Henrard, L.; Anglaret, E.; Sauvajol, J.-L. Diffraction by Finite Size Crystalline Bundles of Single Wall Nanotubes. *Eur. Phys. J. B* **1999**, *10*, 263−270.

(27) Maillet, P.; Levard, C.; Spalla, O.; Masion, A.; Rose, J.; Thill, A. Growth Kinetic of Single and Double-Walled Aluminogermanate Imogolite-Like Nanotubes: an Experimental and Modeling Approach. *Phys. Chem. Chem. Phys.* **2011**, *13*, 2682−2689.

(28) MacKenzie, K.; Bowden, M.; Brown, I.; Meinhold, R. Structure and Thermal Transformations of Imogolite Studied by $^{29}$Si and $^{27}$Al High-Resolution Solid-State Nuclear Magnetic Resonance. *Clays Clay Miner.* **1989**, *37*, 317−324.

(29) Kang, D.; Zang, J.; Wright, E.; McCanna, A.; Jones, C.; Nair, S. Dehydration, Dehydroxylation, and Rehydroxylation of Single-Walled Aluminosilicate Nanotubes. *ACS Nano* **2010**, *4*, 4897−4907.

(30) Thess, A.; Lee, R.; Nikolaev, P.; Dai, H.; Petit, P.; Robert, J.; Xu, C.; Lee, Y.; Kim, S.; Rinzler, A.; et al. Crystalline Ropes of Metallic Carbon Nanotubes. *Science* **1996**, *273*, 483.

(31) Gustafsson, J. The Surface Chemistry of Imogolite. *Clays Clay Miner.* **2001**, *49*, 73−80.

(32) Zhao, M.; Xia, Y.; Mei, L. Energetic Minimum Structures of Imogolite Nanotubes: A First Principles Prediction. *J. Phys. Chem. C* **2009**, *113*, 14834−14837.

(33) Farmer, V.; Fraser, A.; Tait, J. Characterization of the Chemical Structures of Natural and Synthetic Aluminosilicate Gels and Sols by Infrared Spectroscopy. *Geochim. Cosmochim. Acta* **1979**, *43*, 1417−1420.

(34) Clark, C.; McBride, M. Cation and Anion Retention by Natural and Synthetic Allophane and Imogolite. *Clay Miner.* **1984**, *32*, 291−299.

9305

dx.doi.org/10.1021/jp5029678 | *J. Phys. Chem. C* 2014, 118, 9299−9306

(35) Paineau, E.; Albouy, P.-A.; Rouzière, S.; Orecchini, A.; Rols, S.; Launois, P. X-ray Scattering Determination of the Structure of Water during Carbon Nanotube Filling. *Nano Lett.* **2013**, *13*, 1751−1756.

(36) Cambedouzou, J.; Pichot, V.; Rols, S.; Launois, P.; Petit, P.; Klement, R.; Kataura, H.; Almairac, R. On the Diffraction Pattern of $C_{60}$ Peapods. *Eur. Phys. J. B* **2004**, *42*, 31−45.

(37) Launois, P.; Chorro, M.; Verberck, B.; Albouy, P.-A.; Rouzière, S.; Colson, D.; Forget, A.; Noé, L.; Kataura, H.; Monthioux, M.; et al. Transformation of $C_{70}$ Peapods into Double Walled Carbon Nanotubes. *Carbon* **2010**, *48*, 89−98.

(38) Tersoff, J.; Ruoff, R. Structural Properties of a Carbon-Nanotube Crystal. *Phys. Rev. Lett.* **1994**, *73*, 676−679.

(39) Tang, J.; Qin, L.-C.; Sasaki, T.; Yudasaka, M.; Matsushita, A.; Iijima, S. Compressibility and Polygonization of Single-Walled Carbon Nanotubes under Hydrostatic Pressure. *Phys. Rev. Lett.* **2000**, *85*, 1887−1889.

(40) Lopez, M.; Rubio, A.; Alonso, J.; Qin, L.-C.; Iijima, S. Novel Polygonized Single-Wall Carbon Nanotube Bundles. *Phys. Rev. Lett.* **2001**, *86*, 3056.

(41) Sluiter, M. H.; Kawazoe, Y. Phase Diagram of Single-Wall Carbon Nanotube Crystals under Hydrostatic Pressure. *Phys. Rev. B* **2004**, *69*, 224111.

(42) San Miguel, A. Nanomaterials under High Pressure. *Chem. Soc. Rev.* **2006**, *35*, 876−889.

(43) Motta, M.; Moisala, A.; Kinloch, I.; Windle, A. High-Performance Fibres from "Dog Bone" Carbon Nanotubes. *Adv. Mater.* **2007**, *19*, 3721−3726.

(44) Yucelen, G. I.; Choudhury, R. P.; Leisen, J.; Nair, S.; Beckham, H. W. Defect Structures in Aluminosilicate Single-Walled Nanotubes: A Solid-State Nuclear Magnetic Resonance Investigation. *J. Phys. Chem. C* **2012**, *116*, 17149−17157.